JMEPEG (2019) 28:2489–2498
https://doi.org/10.1007/s11665-019-04031-0

1059-9495/$19.00

Comparison of the Phase Stability and Corrosion Resistance of the Ni-Based Alloys C-4 and C-276

H.M. Tawancy and L.M. Alhems

(Submitted November 20, 2018; in revised form January 20, 2019; published online April 12, 2019)

A one-to-one correspondence is developed between the phase stability and corrosion resistance of the commercial (Ni-Cr-Mo)-based alloys C-276 and C-4. Alloy C-4 is shown to outperform alloy C-276 in acidic oxidizing media and approaches its resistance in acidic reducing media. Both alloys are found to have similar resistance to chloride-induced stress corrosion cracking in the annealed condition with short-range order. The aqueous corrosion resistance of both alloys is found to be improved by long-range order; however, they become highly susceptible to chloride-induced stress corrosion cracking. Alloy C-4 is distinguished by being stable toward precipitation of detrimental intermetallic compounds. However, alloy C-276 is shown to be prone to precipitation of mu phase which degrades its resistance to aqueous corrosion and chloride-induced stress corrosion cracking. It is concluded that the chemical composition of alloy C-4 is tailored to make it more versatile than alloy C-276 in acidic oxidizing media and the results are found to be consistent with the concept of atomic percent factor of each alloy.

Keywords aqueous corrosion, electron microscopy, microstructure, Ni-based alloys, stress corrosion cracking

1. Introduction

Proper selection of engineering alloys for applications involving exposure to corrosive environments is of utmost importance in reducing maintenance and repair costs as well as unscheduled plant shutdowns. In this regard, various versions of corrosion-resistant alloys based upon the Ni-Cr-Mo system (Ref 1) have long been used in many applications as structural materials for process equipment used in the petrochemical (Ref 2) and chemical process (Ref 3, 4) industries. This is attributed to their potentially useful combination of corrosion resistance to wide range of both acidic oxidizing and reducing media as well as mechanical strength and ease of fabrication. Alloys of commercial grades in this category include the popular Hastelloy alloys C-276 and C-22 which have been the subject of many studies. Most of these studies, however, have focused on the electrochemical aspect of corrosion with less emphasis on microstructure particularly on the fine scale of transmission electron microscopy (Ref 5-15). Also, in these studies, Hastelloy alloy C-4 has received much less attention as compared to the other members of the C-family of alloys.

Commercial-grade alloys in the above category are fabricated by the manufacturers into wrought products (sheets, plates, bars, etc.) and given a prescribed annealing treatment. This condition is sometimes referred to as mill-annealed. Being complex multi-component alloy systems, the mill-annealed microstructure exists in a thermodynamically metastable condition. Exposure to elevated temperatures such as occurrence during thermo-mechanical processing of hardware items or during service can promote different microstructural changes which alter the initial properties including resistance to corrosive environments. Examples of these changes include precipitation of secondary phases such as carbides and intermetallic compounds as well as disorder-to-order transitions (Ref 16). Inadequate knowledge about the relationship between such microstructural changes and corrosion resistance can in some cases lead to costly component failure (Ref 17-19). It is then evident that for better use and selection of existing alloys and developing new alloys with better properties, it is important to characterize the influence of microstructure on corrosion resistance. Toward this objective, the present investigation has been undertaken to determine the effect of microstructural changes on the resistance to aqueous corrosion and stress corrosion cracking of alloy C-4 in comparison with alloy C-276.

2. Experimental Procedure

Sheet (1 mm thick) and plate (6 mm thick) from the same heats of alloys C-276 and C-4 were included in the investigation. All samples were heat-treated as recommended by the manufacturer (C-276: 20 min/1120 °C/water quenching; C-4: 20 min/1065 °C/water quenching) (Ref 20). Table 1 illustrates the compositions of the alloy heats used in the investigation as determined by inductively coupled plasma-atomic emission spectroscopy except for the C concentration which was determined by combustion calorimetry. For comparative purposes, the nominal compositions of the alloys are also shown in Table 1. It is emphasized that all the data presented in this paper pertain to the two heats of alloys C-276 and C-4 with the compositions listed in Table 1. Commercial-grade alloys are defined by ranges of compositions as indicated by the respective nominal compositions listed in Table 1. Therefore,

H.M. Tawancy and **L.M. Alhems**, Center for Engineering Research, Research Institute, King Fahd University of Petroleum and Minerals, P.O. Box 1639, Dhahran 31261, Saudi Arabia. Contact e-mail: tawancy@kfupm.edu.sa.

heats with different compositions within the specified ranges may have different behaviors.

Thermal exposure tests were carried out at temperatures in the range of 400-1000 °C for different times. Extended exposure up to 100 h was carried out at lower temperatures in the range of 500-650 °C where the Ni-Cr-Mo alloys can undergo long-range ordering reactions (LRO); however, only short-term exposure up to 8 h at higher temperatures can cause precipitation of intermetallic compounds with rapid kinetics (Ref 16).

Aqueous 24-h immersion tests were carried out on annealed and aged specimens (25.4 × 25.4 × 1 mm) in both acidic oxidizing and reducing media using six specimens for each condition. Isocorrosion diagrams (Ref 8) were generated from the two alloys in acidic oxidizing (HNO_3) and acidic reducing (HCl) acids to determine the corrosion rates as functions of temperature and acid concentration. Additional tests to determine the comparative resistance in highly oxidizing medium were carried out in boiling 50 wt.% H_2SO_4 + 42 g/L $Fe_2(SO_4)_3$ according to ASTM standard G 28A (Ref 21). Tests in reducing medium were carried out in boiling 10 wt.% HCl according to ASTM standard G 31 (Ref 21). Weight change measurements of specimens before and after the tests were used to determine the respective corrosion rates using the formula mpy = 534 W/DAT, where mpy is the corrosion rate in mils/year (mm/year = mils/40), W is the weight change in milligram, D is the density of the material in gm/cm^3, A is the surface area of the specimen in inch^2, and T is the exposure time in hours (Ref 22). All acid concentrations throughout the text are given in wt.%.

Chloride-induced stress corrosion cracking (SCC) tests were carried out on plate specimens in the annealed and aged conditions according to ASTM standard G 36-94 (Ref 23) and using three specimens for each condition. The specimens were bent and held at constant strain of 7% in boiling 45% $MgCl_2$ (154 °C) for 200 h. Room temperature tensile tests (sheet specimens with 50.8 mm gage length) were carried out to characterize the deformation substructure which provides important information about the resistance to stress corrosion cracking.

Detailed microstructural characterization was carried out using optical microscopy, scanning electron microscopy (SEM) and transmission electron microscopy (TEM) combined with energy-dispersive spectroscopy (EDS) for microchemical analysis. Specimens for optical microscopy used to reveal the gross grain structure were etched in a solution consisting of 80% HCl and 20% chromic acid with concentration of 15 mol.%. Thin foils for TEM experiments were prepared by the jet polishing technique in a solution consisting of 30% nitric acid in methanol. The foils were examined at an accelerating voltage of 200 keV. All electron diffraction patterns throughout the text are indexed in terms of the face-centered cubic structure (fcc) with the exception of the hexagonal structure of mu phase.

Table 1 Chemical compositions of alloys C-276 and C-4 (wt.%)

	C-276		C-4	
Element	**Nominal**	**Measured**	**Nominal**	**Measured**
Ni	Balance	56.34	Balance	62.43
Cr	14.5-16.5	14.98	14-18	17.10
Mo	15-17	15.76	14-17	16.65
W	3-4.5	3.57	...	...
Fe	4-7	6.20	3(a)	1.49
Co	2.5(a)	1.89	2(a)	1.26
Mn	1(a)	0.73	1(a)	0.61
Ti	...	...	0.7(a)	0.14
Si	0.08(a)	0.05	0.08(a)	0.04
V	0.35(a)	0.15	...	...
Cu	0.5(a)	0.22	0.5(a)	0.18
C	0.01(a)	0.09	0.01(a)	0.08
P	0.025(a)	0.01	0.025(a)	0.01
S	0.01(a)	0.01	0.01(a)	0.01

(a) Maximum

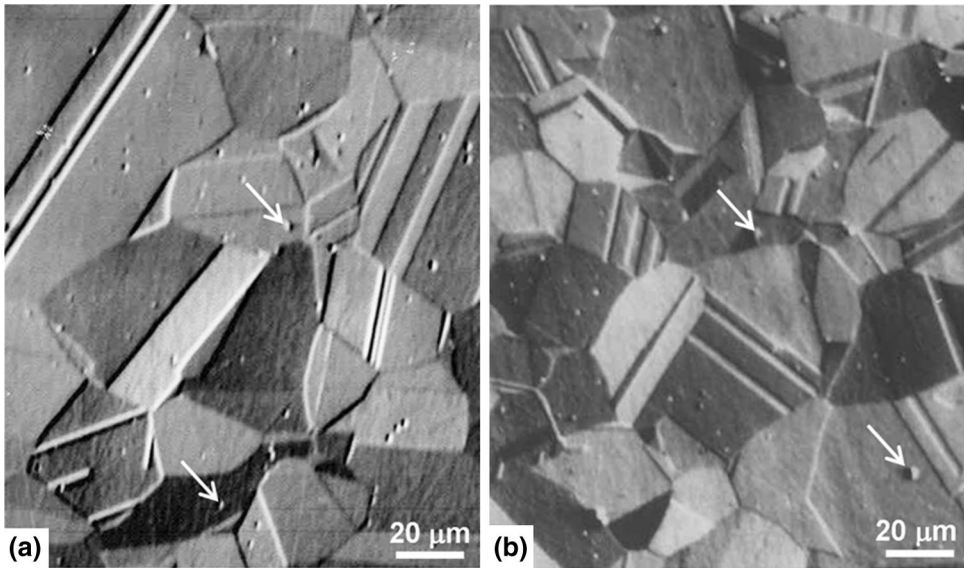

Fig. 1 Optical micrographs illustrating the gross grain structures of alloy C-276 (a) and alloy C-4 (b) in the annealed condition; secondary phase particles are indicated by the arrows

3. Results and Discussion

3.1 Microstructure and Corrosion Resistance in the Annealed Condition

Figure 1 illustrates characteristic microstructural features of alloy C-276 (Fig. 1a) and C-4 (Fig. 1b) in the annealed condition. The grain structure of each alloy with fcc structure is observed to contain small density of secondary phase particles as indicated by the arrows. These particles are identified to be carbides of the M_6C-type (cubic; $a \approx 1.1$ nm) as exemplified in Fig. 2. As an example, Fig. 2(a) shows a bright-field TEM image of a particle in alloy C-276. A corresponding microdiffraction pattern in [111] orientation is shown in Fig. 2(b). The elemental composition of the particle is shown in the EDS spectrum of Fig. 2(c) where its major

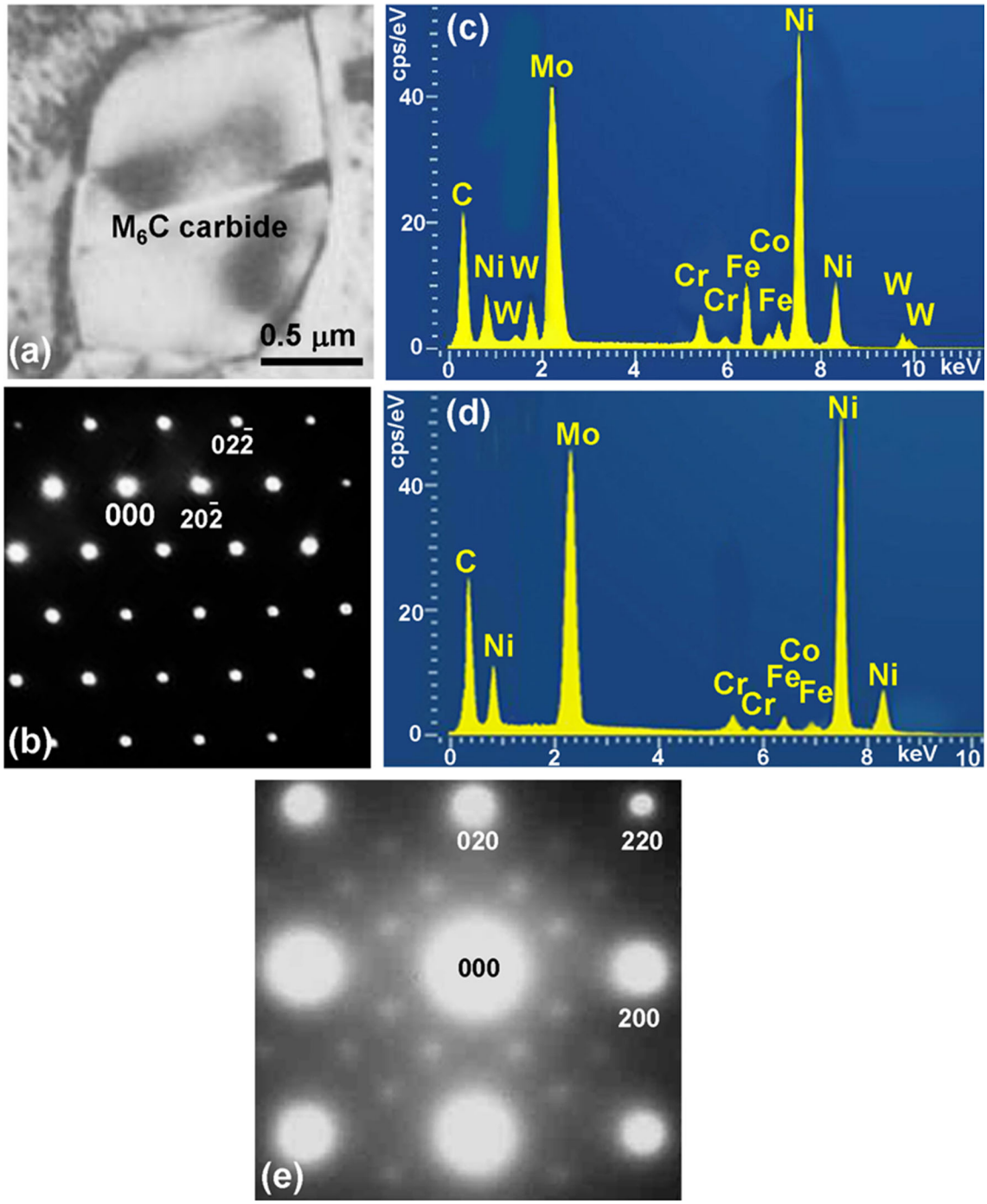

Fig. 2 Characterization of the fine structure in the annealed condition. (a) An example showing a bright-field TEM image of second phase particle in alloy C-276. (b) A corresponding microdiffraction pattern consistent with the cubic structure of the Mo/W-rich M_6C-type carbide. (c) EDS spectrum showing the elemental composition of the carbide particle in (a). (d) EDS spectrum showing the elemental composition of the Mo-rich M_6C carbide in alloy C-4. (e) An example electron diffraction pattern in [001] cubic orientation illustrating the characteristic short-range order reflections at {1 1/2 0} positions

elemental constituents are observed to be Ni and Mo with smaller concentrations of Fe, W and Co. Also in the case of alloy C-4, Ni and Mo are observed to be the major elemental constituents of the M_6C carbide as illustrated in the EDS spectrum of Fig. 2(d). However, consistent with the alloy composition, the carbide phase is observed to be free of W with smaller concentrations of Fe and Cr and Co. Since the M_6C carbide particles are enriched in elements which provide resistance to reducing media, they are expected to act as cathodic regions in reducing tests and become anodic in oxidizing tests (Ref 22). A common feature of the two alloys is found to be the presence of short-range order (SRO) in the annealed condition of the fcc matrix phase similar to the case of binary Ni-Mo alloys (Ref 24). This is reflected by the presence of diffuse reflections at {1 1/2 0} and all equivalent positions in respective electron diffraction patterns. An example is shown in the [001] diffraction pattern of Fig. 2(e). It is noted here that earlier studies have shown that SRO can promote the susceptibility to chloride-induced SCC due to the relationship between SRO and the plastic deformation substructure (Ref 25-27) as further illustrated below.

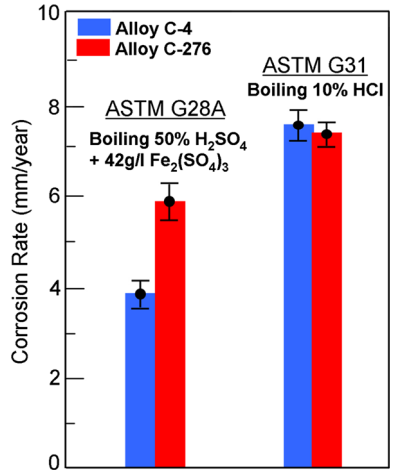

Fig. 5 Comparative resistance to aqueous corrosion of alloys C-276 and C-4 in boiling 50% H_2SO_4 + 42 g/L $Fe_2(SO_4)_3$ and boiling 10% HCl (annealed condition)

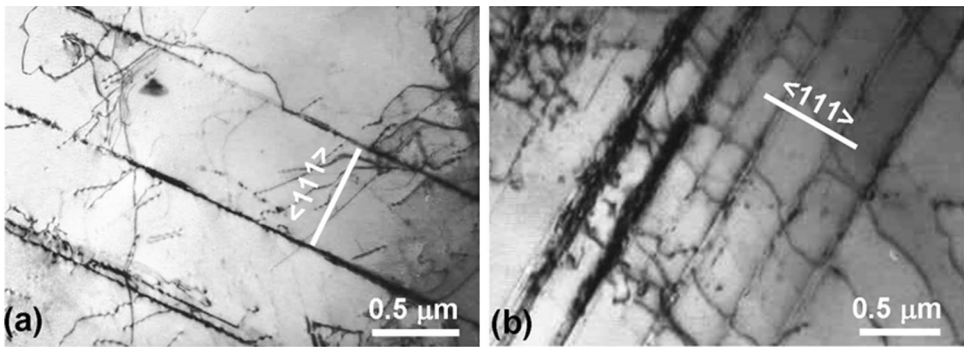

Fig. 3 Bright-field TEM image illustrating the tensile deformation substructure corresponding to 7% elongation in the annealed condition. (a) Alloy C-276. (b) Alloy C-4

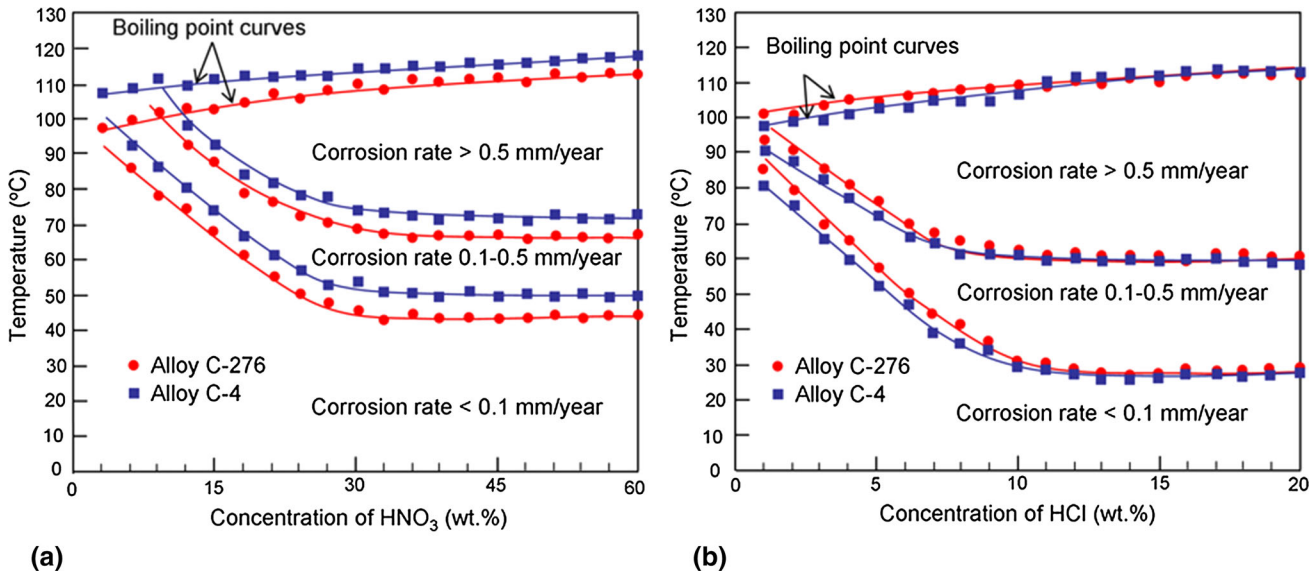

Fig. 4 Isocorrosion diagrams illustrating the comparative resistance to aqueous corrosion of alloys C-276 and C-4 in the annealed condition. (a) Corrosion rates in HNO_3 (acidic oxidizing medium). (b) Corrosion in HCl (acidic reducing medium)

Figure 3 shows bright-field TEM images illustrating the deformation substructure of the two alloys corresponding to 7% tensile elongation at room temperature. It is noted here that this substructure reflects the damage left behind as a result of the respective deformation. Slip lines are visible in both alloys with dislocations confined to their original slip planes with little tendency for cross-slip. Such substructure typifies fcc metals and alloys with low stacking fault energy (Ref 28). In this regard, elements such as Mo and W are well known to lower the stacking fault energy of Ni (Ref 29). Therefore, it is evident that the deformation substructures observed in Fig. 3 are due to the characteristic chemical compositions of both alloys which promote low stacking fault energy as well as SRO which is found to be present after the deformation. However, as shown, later coplanar groupings of dislocations such as those observed in Fig. 3 are necessary, but are not sufficient conditions for higher susceptibility to chloride-induced SCC.

The isocorrosion diagrams of Fig. 4(a) and (b) present an example illustrating, respectively, the comparative resistance of alloys C-276 and C-4 in oxidizing (HNO_3) and reducing (HCl) media. By definition, each line separates the areas representing the combination of temperature and acid concentration where the corrosion rate has the indicated values. Such information can provide a useful tool in selecting alloys for certain applications. It is observed alloy C-4 outperforms alloy C-276 in the oxidizing medium (Fig. 4a) which can be related to its lower content of Mo + W (16.65 wt.% in alloy C-4 and 19.33 wt.% in alloy C-276) and higher Cr content (17.10 wt.% in alloy C-4 and 14.98 wt.% in alloy C-276). In contrast, alloy C-276 is observed to perform slightly better in the reducing

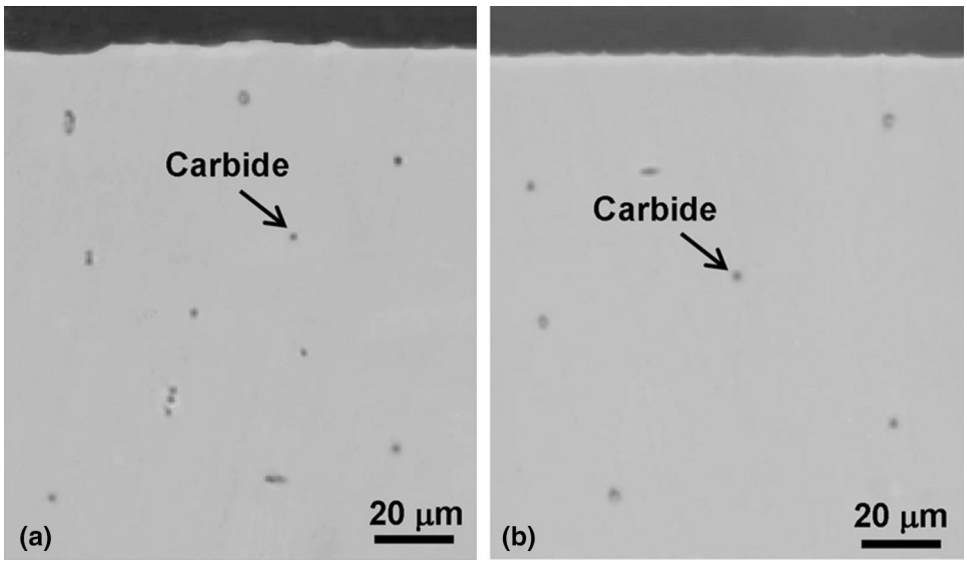

Fig. 6 Secondary electron SEM images illustrating characteristic morphologies along the cross sections after stress corrosion cracking tests in the annealed conditions. (a) Alloy C-276. (b) Alloy C-4

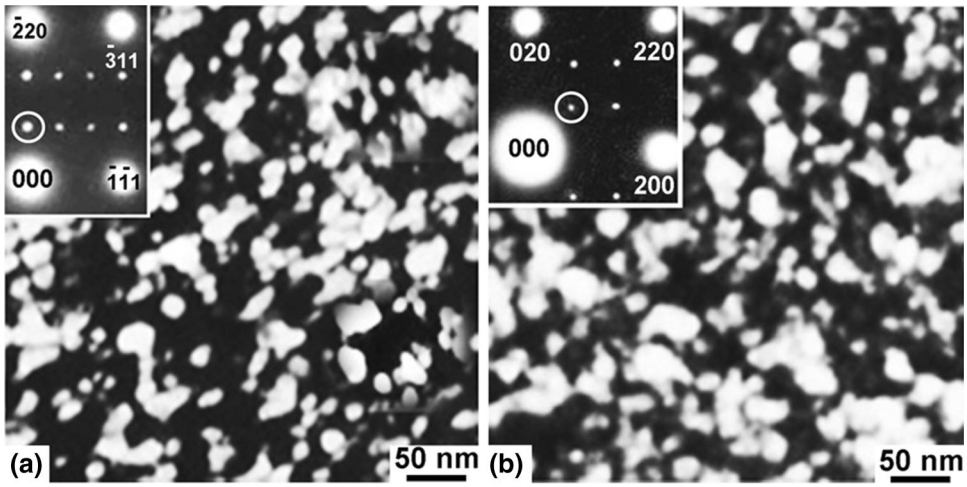

Fig. 7 Dark-field TEM images illustrating the microstructure of the ordered Ni_2(Cr, Mo) phase after 100 h of aging at 650 °C. (a) Alloy C-276; the inset is a diffraction pattern in [112] cubic orientation where the encircled superlattice reflection is used to form the image. (b) Alloy C-4; the inset is a diffraction pattern in [001] orientation where the encircled superlattice reflection is used to form the image

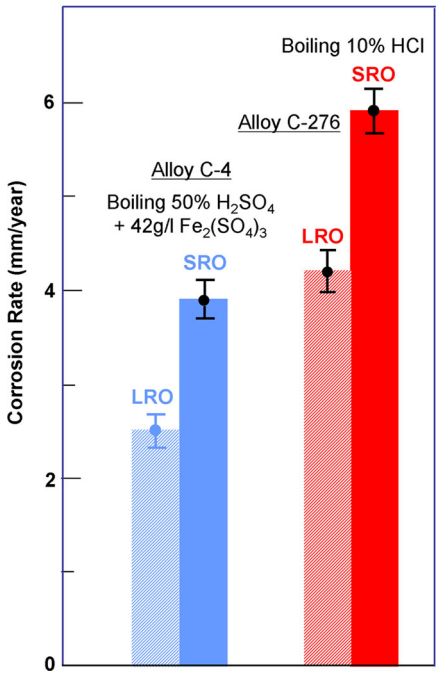

Fig. 8 Comparative corrosion rates of alloys C-276 and C-4 in the short-range order (annealed) and long-range order (100 h at 650 °C) states

medium (Fig. 4b) due to its higher content of Mo + W and lower Cr content. It is noted here that W is much less effective than Mo in its resistance to reducing media (Ref 22). The results of additional tests according to ASTM standards and illustrating comparative resistance of both alloys in various media are summarized in Fig. 5. In the highly oxidizing test specified in ASTM G28A {boiling 50% H_2SO_4 + 42 g/L $Fe_2(SO_4)_3$}}, alloy C-4 is observed to outperform alloy C-276. On the other hand, it is observed that in the reducing test (boiling 10% HCl), the resistance of alloy C-4 closely approaches that of alloy C-276.

Despite the presence of SRO in both alloys (Fig. 2d) as well as the coplanar groupings of dislocations (Fig. 4), none of the three specimens from each alloy has developed cracks after chloride-induced SCC tests according to ASTM standard G 36-94. Figure 6(a) and (b) show, respectively, secondary electron SEM images along cross sections of tested specimens of alloys C-276 and C-4. It is noted here that it has been proposed in an earlier study that transgranular stress corrosion cracks in SRO alloys are developed by localized chemical attacks of the regions of slip planes where SRO is destroyed (Ref 25). Evidently, the persistence of SRO in the present case has enhanced the resistance to localized chemical attack and in turn the resistance to chloride-induced SCC. This is consistent with the observation that the beneficial effect of atomic order on the resistance to aqueous corrosion is realized in the state of long-range order (LRO) as demonstrated below.

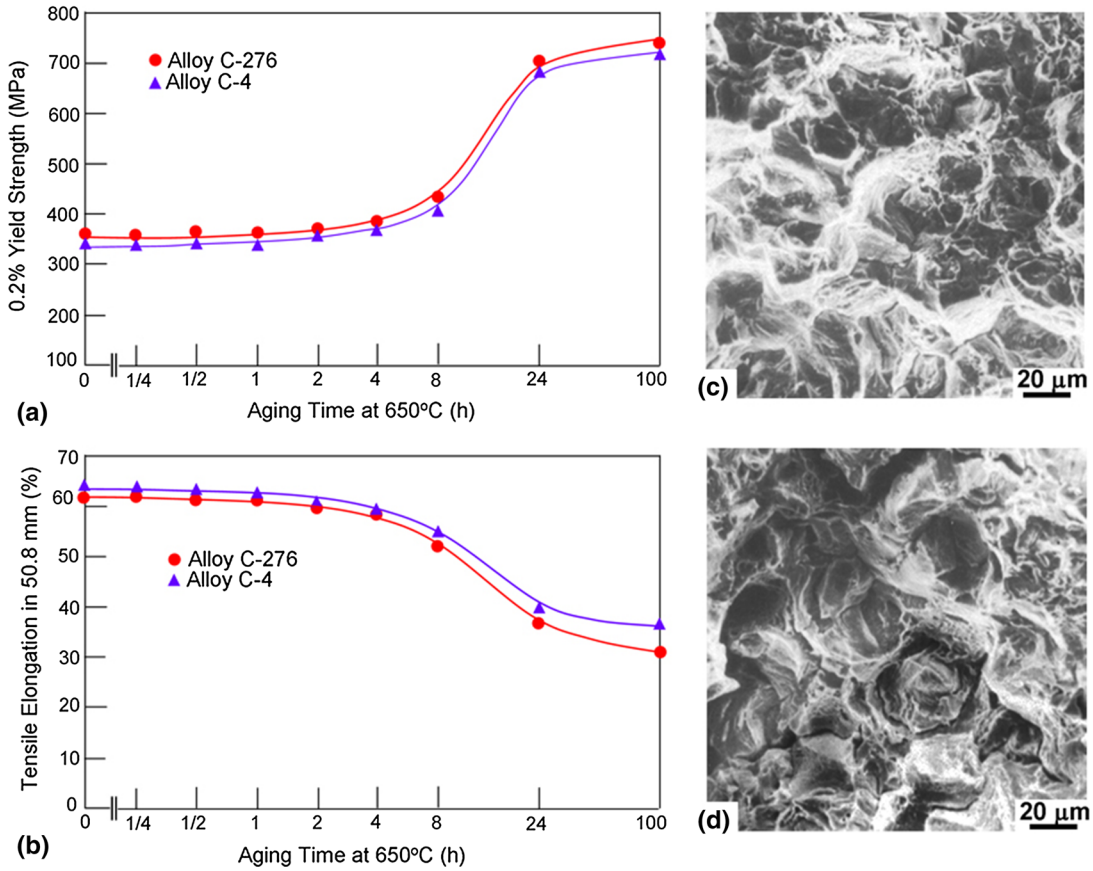

Fig. 9 Effect of long-rang order on the tensile strength and susceptibility to chloride-induced stress corrosion cracking of alloys C-276 and C-4. (a) and (b) shows comparative effects of aging time up to 100 h at 650 °C on the room temperature 0.2% yield strength and tensile ductility, respectively. (c) and (d) shows secondary electron SEM images illustrating the morphologies of surfaces exposed by fracture during the chloride-induced stress corrosion cracking tests in the long-range order states (100 h of aging at 650 °C) of alloys C-276 and C-4, respectively

3.2 Transition from Short-Range to Long-Range Order

A transition from the state of SRO into LRO is observed in the two alloys after extended thermal exposure at temperatures in the range of about 500-700 °C. As a result, the parent fcc structure is transformed into a Pt_2Mo-type superlattice with tetragonal structure and $Ni_2(Cr, Mo)$-based composition. Since the atomic concentrations of Ni, Cr and Mo in the two alloys approach that of $Ni_2(Cr, Mo)$, the transition occurs in a homogeneous manner where the tetragonal is derived from the fcc structure by minor atoms rearrangement on the {420} planes such that every third plane is occupied by Ni atoms and planes in-between contain Cr and Mo atoms (Ref 30). Therefore, a one-to-one correspondence exists between atomic planes and directions in the two structures. In this case, the ordered structure is identified by the observation of superlattice reflections at 1/3{420} and all equivalent positions, which are equivalent to all 1/3{220} positions in the diffraction patterns. This is illustrated in Fig. 7(a) and (b) which shows, respectively, dark-field TEM images and corresponding diffraction patterns of the ordered phase in alloys C-276 and C-4, respectively. Each image is formed with the encircled superlattice reflection in the diffraction patterns of the insets [[112] orientation in Fig. 7(a) and [001] orientation in Fig. 7(b)].

For both alloys, the transition from SRO to LRO is found to improve the resistance to aqueous corrosion as demonstrated in Fig. 8. It is observed that the corrosion rate in the oxidizing medium of boiling 50% H_2SO_4 + 42 g/L $Fe_2(SO_4)_3$ is substantially reduced in the ordered state. In general, this is likely to be associated with the tighter binding forces in ordered alloys and intermetallic compounds (Ref 31). However, LRO is found to degrade the resistance to chloride-induced SCC of both alloys despite the observation that the order-induced strengthening is accompanied by relatively high tensile ductility ranging from about 30-35% as illustrated in Fig. 9(a) and (b). All three specimens tested from each alloy have fractured with mixed transgranular and intergranular modes as illustrated in the secondary electron SEM images of Fig. 9(c) and (d). This behavior can be related to the change in deformation mode from motion and multiplication of dislocations in the SRO state (Fig. 3) into twinning in the LRO state as illustrated in the example Fig. 10. A bright-field TEM image illustrating the deformation substructure corresponding to 7% elongation at room temperature is shown in Fig. 10(a). The corresponding diffraction pattern (Fig. 10b) is characteristic of twinned fcc crystals on {111} planes as viewed in [110] orientation. Furthermore, the characteristic reflections of the Pt_2Mo-type

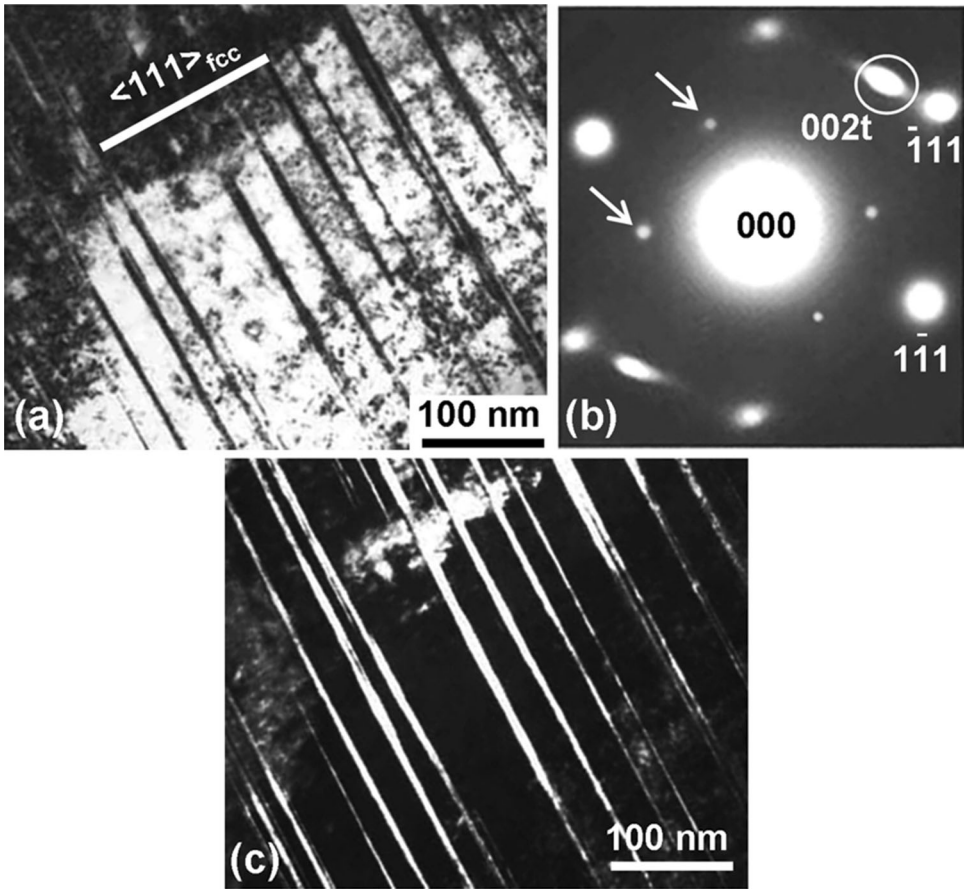

Fig. 10 An example illustrating deformation by twinning in the long-range order state (alloy C-276 given 7% tensile elongation at room temperature after 100 h of aging at 650 °C). (a) Bright-field TEM image. (b) Corresponding twinned diffraction pattern in [110] orientation; the Pt_2Mo-type superlattice reflections are indicated by the arrows). (c) Corresponding dark-field TEM image formed with the encircled (002) twin reflection in (a)

superlattice are also observed which indicates that deformation by twinning preserves the state of LRO. A dark-field TEM image formed with the encircled (002) twin reflection in (b) is shown in Fig. 10(c). It is evident that deformation by twinning creates a high density of internal interfaces which can be subjected to chemical attack resulting in transgranular cracks. It is also likely that a similar behavior may occur at the intersections between twin boundaries and grain boundaries which can explain the occurrence of the mixed fracture modes observed in Fig. 9.

3.3 Precipitation of Mu Phase

Short-term thermal exposure at higher temperatures is found to cause precipitation of mu phase in alloy C-276 which has A_7B_6-type composition where A corresponds to Ni and/or Fe and B corresponds to Mo and W (Ref 16). An example is given in Fig. 11. A blocky particle of mu phase is shown in the bright-field TEM image of Fig. 11(a). The inset is a corresponding diffraction pattern consistent with the hexagonal structure of mu phase in [0001] orientation with a = 0.48 nm and c = 2.58 nm. Due to the complex superlattice of mu phase, it contains various types of planar defects such as twins, stacking faults and antiphase boundaries which give rise to the characteristic internal structure observed in Fig. 11(a). Figure 11(b) shows an EDS spectrum illustrating the elemental composition of the particle in Fig. 11(a). It is observed that Ni and Mo are the major elemental constituents with smaller concentrations of Fe and W, and minor amounts of Cr and Co. In contrast, alloy C-4 is found to have higher stability toward precipitation of mu phase and other intermetallic compounds after at least 1000 h of aging at 900 °C. This behavior can be related to the absence of W in alloy C-4 as well as the smaller concentrations of Fe and Mo (Table 1) and is reflected on the aqueous corrosion resistance the of the two alloys. Furthermore, because of the detrimental effect of mu phase on tensile ductility as illustrated in Fig. 11(c) (12% room temperature tensile elongation for alloy C-276 versus 46% for alloy C-4 after 8 h of aging at 900 °C), alloy C-276 becomes highly susceptible to stress corrosion cracking.

Figure 12(a) and (b) shows, respectively, the effect of 8 h of aging as function of temperatures in the range of 400-1000 °C on the corrosion rates of alloy C-276 and C-4 in acidic oxidizing {boiling 50 wt.% H_2SO_4 + 42 g/L $Fe_2(SO4)_3$) and acidic reducing (boiling 10% HCl) media. In both tests, alloy C-276 is differentiated by the accelerated corrosion rates at temperatures higher than about 700 °C and reaching a maximum value at a temperature between 850 and 900 °C, which can be correlated with precipitation of mu phase. Similar to the case of M_6C carbide, the (Mo + W)-rich mu phase particles are expected to act as cathodic regions in reducing tests and anodic in oxidizing tests. In contrast with alloy C-276, aging at the

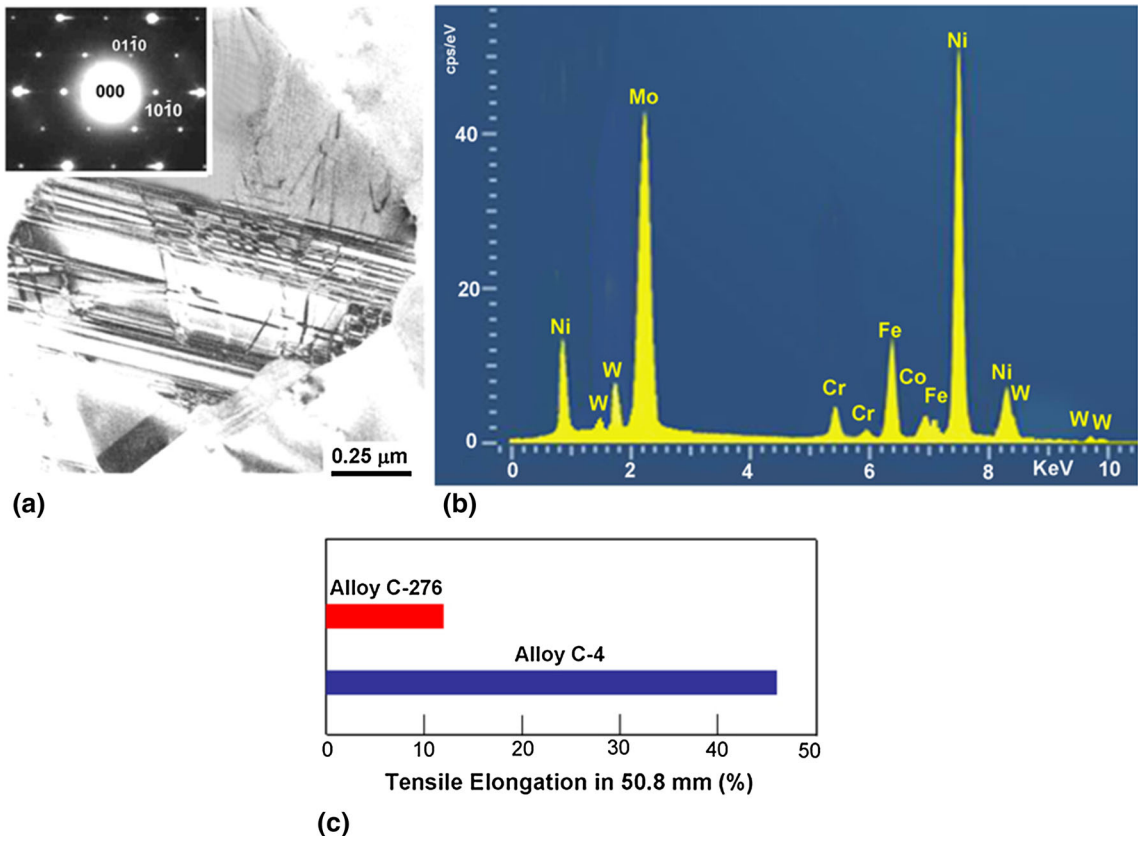

Fig. 11 Identification of mu phase in alloy C-276 after 8 h of aging at 900 °C. (a) Bright-field TEM image illustrating the characteristic internal structure of mu phase; the inset is corresponding diffraction pattern consistent with the hexagonal structure of mu phase in [0001] orientation. (b) Corresponding EDS spectrum illustrating the elemental composition of mu phase. (c) Effect of 8 h of aging at 900 °C on the room temperature tensile ductility of alloys C-276 and C-4

entire temperature range is observed to have no marked effect on the corrosion rates of alloy C-4 which demonstrates its higher thermal stability. As an example, Fig. 13 shows optical micrographs along cross sections of alloys C-276 and C-4 after testing in the above reducing medium. Extensive intergranular attack is observed in the case of alloy C-276 (Fig. 13a), while alloy C-4 is observed to maintain its structural integrity after the test. Also, while all three specimens of alloy C-276 have fractured in the chloride-induced SCC test, no cracking has been detected in the case of alloy C-4 after 8 h of aging at 900 °C.

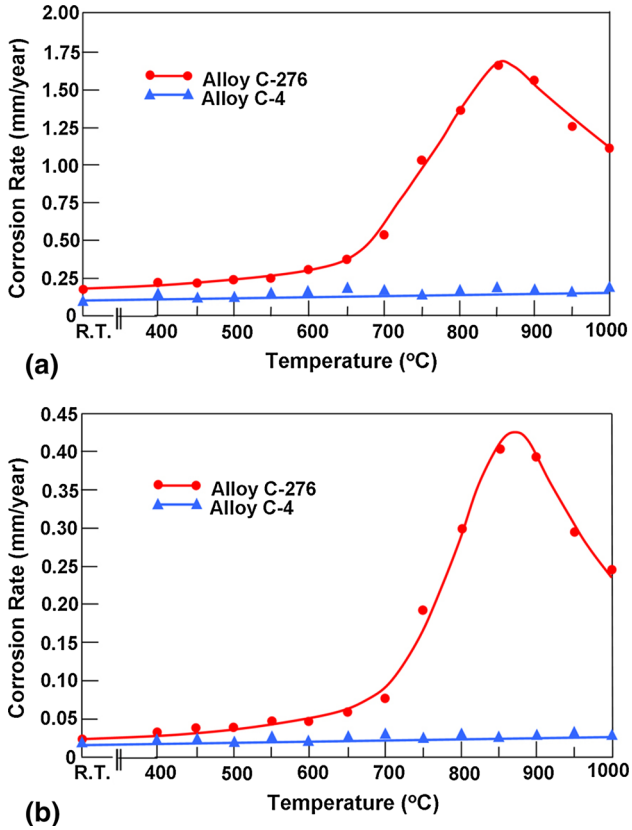

Fig. 12 Effect of 8 h of aging as a function of temperature on the resistance to aqueous corrosion of alloys C-276 and C-4. (a) Boiling 50% H_2SO_4 + 42 g/L $Fe_2(SO_4)_3$. (b) Boiling 10% HCl

3.4 Correlation Between the Atomic Percent Factor and Corrosion Resistance

As demonstrated by the above results, the corrosion resistance of alloy C-4 outperforms that of alloy C-76 in acidic oxidizing media and approaches that of alloy C-276 in acidic reducing media. This is found to be consistent with the atomic percent factor (APF) which is developed to express the opposing effect of Cr (resistance to oxidizing media) on corrosion resistance as compared to that of Mo and W (resistance to reducing media) and has also been used in alloy design (Ref 32, 33). Based upon the relative ratios of atomic weights of Cr (52): Mo (96): W (184), the APF is expressed as:

$$\text{APF} = 4 \times \text{wt.\% Cr}/(2 \times \text{wt.\% Mo} + 1 \times \text{wt.\% W}).$$

The resistance to oxidizing acids increases with an increase in APF, and a smaller value of APF reflects lower resistance to reducing acids. Reference to the actual compositions of alloys C-276 and C-4 listed in Table 1, the values are determined to be:

APF of alloy C-276 = 1.71
APF of alloy C-4 = 2.05

Therefore, the APF predicts that alloy C-4 outperforms alloy C-276 in oxidizing acids and approaches that of alloy C-276 in reducing acids consistent with the results of the present study.

4. Conclusions

It is concluded from the present investigation that in the annealed condition with short-range order, alloy C-4 exhibits higher resistance to acidic oxidizing media and approaches the

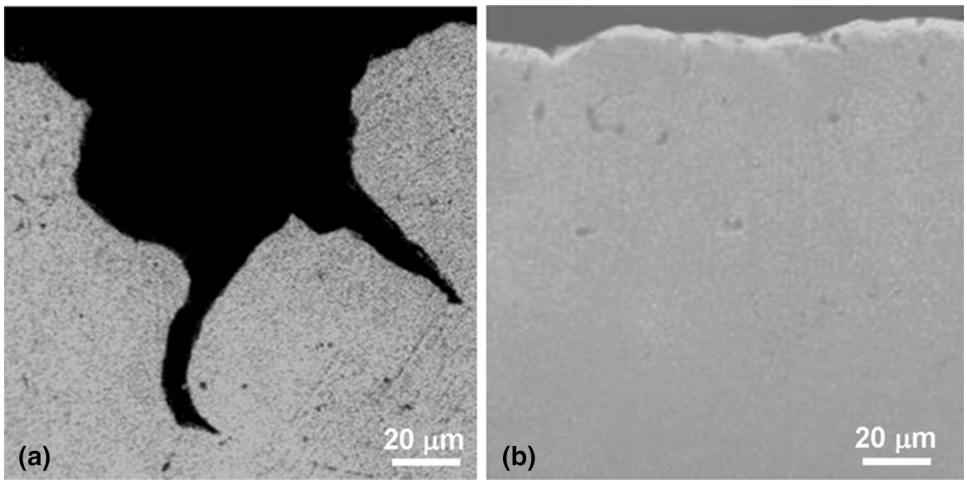

Fig. 13 Optical micrographs along cross sections of alloy C-276 (a) and C-4 (b) after 8 h of aging at 900 °C followed by corrosion testing in boiling 50% H_2SO_4 + 42 g/L $Fe_2(SO_4)_3$

resistance provided by alloy C-276 in acidic reducing media. However, in that condition, both alloys show similar resistance to stress corrosion cracking. Although the transition from short-range to long-range order after aging at temperatures in the range of 550-650 °C is found to improve the corrosion resistance of both alloys, their resistance to stress corrosion cracking is degraded. In contrast with alloy C-276 which is susceptible to precipitating detrimental intermetallic compounds particularly mu phase after aging at higher temperatures with adverse effects on aqueous corrosion resistance and resistance to stress corrosion cracking, alloy C-4 maintains higher stability toward precipitating such compounds. The advantages of alloy C-4 over alloy C-276 are correlated with its chemical composition which is adjusted to produce microstructure with enhanced corrosion resistance particularly in acidic oxidizing environments. The results are found to be consistent with the concept of atomic percent factor of each alloy.

Acknowledgments

It is a pleasure to acknowledge the continued support of King Fahd University of Petroleum and Minerals.

References

1. P. Crook, Corrosion Characteristics of the Wrought Ni-Cr-Mo Alloys, *Mater. Corros.*, 2005, **56**, p 606–610
2. V. Burt, *Corrosion in the Petrochemical Industry*, 2nd ed., ASM International, Materials Park, 2015, p 75–81
3. P. Crook, Corrosion-Resistant Nickel Alloys: Part II, *Adv. Mater. Process.*, 2007, **56**, p 31–33
4. D.C. Agarwal and W.R. Herda, The "C" Family of Ni-Cr-Mo Alloys' Partnership with the Chemical Process Industry: The Last 70 Years, *Mater. Corros.*, 1997, **48**, p 542–548
5. H. Shi, Z. Gao, Z. Fan, and Y. Ding, Corrosion Behavior of Alloy C-276 in Supercritical Water, *Adv. Mater. Sci. Eng.*, 2018, **2018**, art. no. 1027640
6. S. Lee, M.J. Kim, J. Park, S.Y. Hwang, S.W. Chung, S.J. Lee, and Y. Yun, Corrosion Behavior of Hastelloy (R) C-4 (R) Ni-Cr-Mo-Fe Alloys for Coal Gasification Syngas Plants, *Mater. Test.*, 2018, **60**, p 156–162
7. C.C. Sequeira, D.S.P. Cardoso, L. Amaral, B. Sljukic, and D.M.F. Santos, On the Performance of Commercially Available Corrosion-Resistant Nickel Alloys: A Review, *Corros. Rev.*, 2016, **34**, p 187–200
8. A. Mishra, Performance of Corrosion-Resistant Alloys in Concentrated Acids, *Acta Metall. Sin. (Engl. Lett.)*, 2017, **30**, p 306–318
9. A.N. Arjomand, I. Petrushina, A. Nikiforov, J.O. Jensen, and M. Rokni, Corrosion Behavior of Construction Materials for Ionic Liquid Hydrogen Compressor, *Int. J. Hydrogen Energy*, 2016, **41**, p 16688–16695
10. X. Tang, S. Wang, L.L. Qian, Y.H. Li, Z.H. Lin, D.H. Xu, and Y.P. Zhang, Corrosion Behavior of Nickel Base Alloys, Stainless Steel and Titanium Alloy in Supercritical Water Containing Chloride, Phosphate and Oxygen, *Chem. Eng. Res. Des.*, 2015, **100**, p 530–541
11. C.M. Giordano, M.R. Ortiz, M.A. Rodriguez, R.M. Carranza, and R.B. Rebak, Crevice Corrosion Testing Methods for Measuring Repassivation Potential of Alloy C-22, *Corros. Eng. Sci. Technol.*, 2011, **46**, p 129–133
12. N.S. Zadorozne, M.A. Rodriguez, R.M. Carranza, Corrosion resistance of Ni-Cr-Mo and Ni-Mo-Cr alloys in different metallurgical conditions. NACE corrosion 2010, paper no. 10236
13. Q. Zhang, R. Tang, K.J. Yin, X. Luo, and L.F. Zhang, Corrosion Behavior of Hastelloy C-276 in Supercritical Water, *Corros. Sci.*, 2009, **51**, p 2092–2097
14. A.C. Lloyd, J.J. Noel, S. McIntyre, and D.W. Shoesmith, Cr, Mo and W Alloying Additions in Ni and Their Effect on Passivity, *Electrochem. Acta*, 2004, **49**, p 3015–3027
15. K.S.E. Al-Malahy and T. Hodgkiess, Comparative Studies of Seawater Corrosion Behavior of a Range of Materials, *Desalination*, 2003, **158**, p 35–42
16. H.M. Tawancy, On the Precipitation of Intermetallic Compounds in Selected Solid-Solution Strengthened Ni-Base Alloys and Their Effects on Mechanical Properties, *Metallogr. Microstruct. Anal.*, 2015, **6**, p 200–215
17. K. Chandra, A. Mahanti, V. Kain, B.S. Kumar, N. Kumar, and V. Gautam, Failure Cases Related to Materials Issue in Wet-Process Phosphoric Acid Plant, *Eng. Fail. Anal.*, 2017, **79**, p 642–655
18. H.M. Shalaby, Failure of Hastelloy C-276 Pump Impeller in Hydrochloric Acid, *Eng. Fail. Anal.*, 2008, **15**, p 543–546
19. R.C. Yin, Y. Al-Bakheet, and A.H. Al-Shawaf, Failure Analysis of an EDC Incinerator Quench Nozzle, *Eng. Fail. Anal.*, 2007, **14**, p 41–46
20. Haynes international heat treatment brochure. http://www.haynesintl.com/alloys/fabrication-brochure/heat-treatment
21. Annual Book of ASTM Standards, vol. 3.02, G 28A, G28 B, G 31 (ASTM International, Conshohocken, 2001)
22. M.G. Fontana and N.G. Greene, *Corrosion Engineering*, McGraw-Hill, New York, 1978, p 116–156
23. ASTM G36-94, *Standard Practice for Evaluating Stress-Corrosion Cracking Resistance of Metals and Alloys in a Boiling Magnesium Chloride Solution*, ASTM International Conshohocken, Pennsylvania, 2013
24. H.M. Tawancy, Correlation Between Disorder-Order Transformations in a Ni-Based Alloy and its Mechanical Properties, *Mater. Sci. Eng. A*, 2018, **719**, p 93–103
25. D.L. Douglass, G. Thomas, and W.E. Roser, Ordering, Stacking Faults and Stress Corrosion Cracking in Austenitic Alloys, *Corrosion*, 1964, **20**, p 15t–28t
26. G. Thomas, The Effect of Short-Range Order on Stacking Fault Energy and Dislocation Arrangements in fcc Solid Solutions, *Acta Met.*, 1963, **11**, p 1369–1371
27. P.R. Swann, Dislocation Substructure vs. Transgranular Stress Corrosion Susceptibility of Single Phase Alloys, *Corrosion*, 1963, **19**, p 102t–114t
28. P.R. Swann, Dislocation arrangements in face-centered cubic metals and alloys, *Electron Microscopy and Strength of Crystals*, G. Thomas and J. Washburn, Ed., Wiley Interscience, New York, 1963, p 131–181
29. C.L. Zacherl, S.L. Shang, D.E. Kim, Y. Wang, and Z.K. Liu, Effects of alloying elements on elastic, stacking fault and diffusion properties of FCC Ni from first-principles: implications for tailoring the creep rate of Ni-base superalloys, *Superalloys 2012: 12th International Symposium on Superalloys*, E.S. Huron, R.C. Reed, M.C. Hardy, M.J. Mills, R.E. Montero, P.D. Portella, and J. Telesman, Ed., The Minerals, Metals and Materials Society, Warrendale, 2012, p 455–461
30. H.M. Tawancy and M.O. Aboelfotoh, Application of Long-Range Ordering in the Synthesis of Nanoscale Ni_2(Cr, Mo) Superlattice with High Strength and High Ductility, *Mater. Sci. Eng. A*, 2009, **500**, p 188–195
31. D. Nguyen-Manh, V. Vitek, and A.P. Horsfeld, Environmental Dependence of Bonding: A Challenge for Modeling of Intermetallics and Fusion Materials, *Prog. Meter. Sci.*, 2007, **52**, p 255–298
32. A. Asphahani, P.E. Manning, and J. Straatmann, New Advances in Molybdenum-Containing Corrosion Resistant Alloys, *Molybd. Moasic*, 1987, **10**, p 1–5
33. N. Sridhar, J.B.C. Wu, and P.E. Manning, Corrosion Resistant Ni-Cr-Mo Alloys, *J. Met.*, 1985, **37**, p 51–53